RESEARCH ARTICLE

60 years of pss

www.pss-rapid.com

Study of Spin Pumping through α-Sn Thin Films

Łukasz Gladczuk, Leszek Gladczuk, Piotr Dluzewski, Gerrit van der Laan, and Thorsten Hesjedal**

Elemental tin in the α-phase is an intriguing member of the family of topological quantum materials. In thin films, with decreasing thickness, α-Sn transforms from a 3D topological Dirac semimetal (TDS) to a 2D topological insulator (TI). Getting access to and making use of its topological surface states is challenging and requires interfacing to a magnetically ordered material. Herein, the successful epitaxial growth of α-Sn thin films on Co, forming the core of a spin-valve structure, is reported. Time- and element-selective ferromagnetic resonance experiments are conducted to investigate the presence of spin pumping through the spin-valve structure. A rigorous statistical analysis of the experimental data using a model based on the Landau–Lifshitz–Gilbert–Slonczewski equation is applied. A strong exchange coupling contribution is found, however no unambiguous proof for spin pumping. Nevertheless, the incorporation of α-Sn into a spin valve remains a promising approach given its simplicity as an elemental TI and its room-temperature application potential.

1. Introduction

Topological insulators (TIs)[1]—a class of materials that are insulating in their bulk and conducting on their surface[2]—hold great promise for revolutionizing spintronics and other fields of emerging electronics. The most remarkable properties of TI states are their protection against backscattering, full spin polarization, very high carrier mobility, and low energy dissipation.[1,3–9] The established and experimentally confirmed binary or ternary TI materials in the $(\mathrm{Bi,Sb})_2(\mathrm{Se,Te})_3$ system have the intrinsic problem of defect-induced bulk conductivity.[10] Elemental tin, in contrast, is a much simpler system that shows a rich topological phase diagram.[11] If properly strained, it can be phase-stabilized and made a room-temperature TI. It is further compatible with established compound semiconductor substrates and quasi-lattice-matched to, e.g., InSb (6.4798 Å) and CdTe (6.4829 Å). α-tin (gray tin) is the low-temperature phase of tin, which has the diamond cubic crystal structure (6.467 Å), a direct bandgap of 0 eV, and a "negative" bandgap of $\Gamma_7 - \Gamma_8 = 0.413$ eV.[12] The bulk transition to β-tin (white tin) above 13.2 °C can be suppressed in thin films by strain engineering,[13] or by adding dopants,[14] to more than 150 °C[15] depending on the substrate orientation.[16] Application of uniaxial stress makes α-Sn a semiconductor as it splits the degenerate Γ_8 state.[17] Due to its simple structure, the material has the potential to show lower defect densities—and thus suppress the unwanted bulk conductivity. Due to its strain and dimensionality-dependent topological properties, α-Sn is a versatile platform for exploring exotic electronic effects.[18] In contrast, suitably, i.e., in terms of size and sign, strained α-Sn films on InSb(111) above a critical thickness have shown 3D-topological Dirac semimetal (TDS) states.[19] On the other hand, for very low thickness α-Sn films on In-terminated InSb(111)A, linearly dispersing 2D topological surface states have been observed.[20] Interestingly, it was found that Fe impurities do not break time-reversal symmetry (TRS) in these systems.[21] The precise thickness at which the 3D to 2D transition occurs depends also on the specific strain state of the films, but was found to be between 30 and 10 Sn bilayers for films investigated by Xu et al.[19]

Interfaces between materials of different topological band character lie at the heart of TI systems as the metallic, spin-polarized states occur only at such interfaces. Breaking TRS in these systems is of great interest and can be achieved by interfacing a TI to a ferromagnet,[22–24] which is the key requirement for observing the quantum anomalous Hall effect (QAHE).[25] Topologically protected surface states can also exert a torque on spins in a neighboring ferromagnet (FM) through exchange coupling,[26] which could serve as a mechanism for all-electrical magnetization switching. Another key phenomenon that has been studied in the context of TIs is spin pumping,[27,28] whereby a pure spin current is

---

Dr. Ł. Gladczuk, Prof. T. Hesjedal
Department of Physics
Clarendon Laboratory
University of Oxford
Oxford OX1 3PU, UK
E-mail: thorsten.hesjedal@physics.ox.ac.uk

Dr. L. Gladczuk, Prof. P. Dluzewski
Institute of Physics
Polish Academy of Science
Aleja Lotnikow 32/46, PL-02668 Warsaw, Poland

Prof. G. van der Laan
Diamond Light Source
Harwell Science and Innovation Campus
Didcot, Oxfordshire OX11 0DE, UK
E-mail: gerrit.vanderlaan@diamond.ac.uk

The ORCID identification number(s) for the author(s) of this article can be found under https://doi.org/10.1002/pssr.202100137.

DOI: 10.1002/pssr.202100137

pumped from an FM layer undergoing ferromagnetic resonance (FMR) into an adjacent layer.[29] Spin pumping is commonly studied via the broadening of the magnetic resonance, whereby it manifests itself as an additional damping term in the magnetodynamic equations.[30] Spin pumping from an Fe layer via Ag into an 30-monolayer-thick α-Sn film had been demonstrated in 2016,[31] which was very recently complemented by the demonstration of spin pumping into its 3D-TDS state.[32] Apart from this indirect way of studying spin currents, direct confirmation can be obtained by pumping the spin current through a nonmagnetic spacer layer into a second FM layer, which is not at resonance.[33] In such a spin-valve structure, the amplitude and phase of the precession of the nonresonant layer are analyzed, allowing for a direct probing of the coupling mechanisms between the layers, and therefore for an unambiguous proof of spin pumping.[34] In this context, TI layers offer exciting prospects given their spin–momentum locked surface states,[35,36] and the investigation of a TI-based spin-valve has been reported earlier.[37]

Here, we explore spin pumping in a spin-valve device incorporating a 2D-TI α-Sn spacer layer. The main experimental challenge is to find a suitable ferromagnet on which the α-phase can be stabilized in thin-film form while straining the material by epitaxy to drive it into the topologically insulating state. We succeeded in growing thin α-Sn on hcp Co(0001), and produced a spin valve by adding an amorphous $Ni_{80}Fe_{20}$ layer (permalloy = Py). We used FMR and time- and element-selective X-ray-based FMR (XFMR)[38] to study spin pumping in the FM–TI–FM spin valves. The element selectivity allows for the probing of the magnetization dynamics of the individual FM layers.[33] Hereby, the phase of dynamic signals is extremely sensitive to the layer coupling in general and spin transfer phenomena in particular. We find no clear evidence for spin pumping through the α-Sn layer, which could be explained by dynamic exchange[39] or by the limited number of current paths in this 2D-TI.

2. Sample Preparation and Characterization

The growth of α-Sn thin films has been achieved on a number of substrates, including Si[40–44] and Ge.[45–48] However, to stabilize the α-phase, InSb(001)[49,50] and Sb-terminated InSb(111)B[15,19] have been shown to be ideally suited, providing a compressive strain of 0.14% in both cases and thus stabilizing the α-phase up to 170 °C.[15] In search for a suitable FM that provides a low-mismatch growth template, we evaluated materials that are compatible with the (111) face of α-Sn. The hexagonal closed-packed (hcp) Co(0001) plane is characterized by a triangular surface mesh with $a_{\mathrm{Co}} = 2.519$ Å[51] (**Figure 1**a). Similarly, the α-Sn(111) plane of the cubic diamond crystal structure is characterized by a triangular mesh with $b_{\mathrm{Sn}} = 4.572$ Å[52] (Figure 1b). By rotating the Sn lattice by 30° with respect to the Co lattice, as shown in Figure 1c with Sn resting in Co hollow sites (giving $b_{\mathrm{Co}} = \sqrt{3}a = 4.364$ Å), a relatively low lattice mismatch of $(b_{\mathrm{Sn}} - b_{\mathrm{Co}})/b_{\mathrm{Sn}} \approx 5\%$ is obtained. Thus, we studied the growth of α-Sn on the hcp Co(0001) surface.

For achieving epitaxial growth of α-Sn on hcp Co(0001), we evaluated several growth approaches for the Co layer. The most successful samples rely on a Au(111)/Mo(110) heterostructure

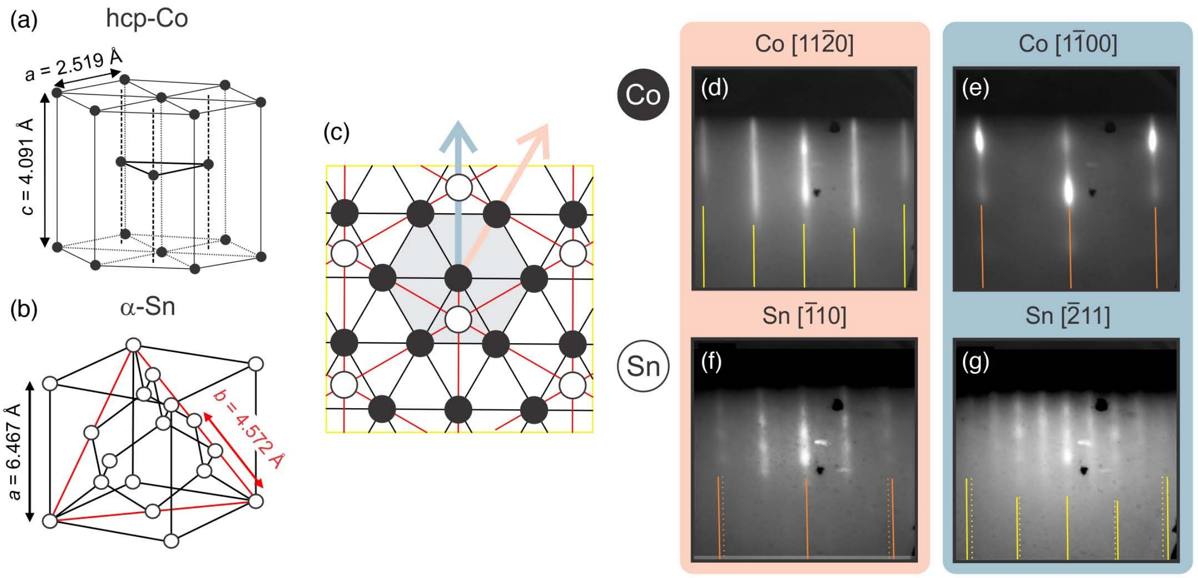

Figure 1. a,b) Crystal structure of hcp Co (a) and cubic α-Sn (b). The Co(0001) plane is the hexagonal basal plane. The α-Sn(111) plane is indicated by a red triangle and the interatomic distance in this plane is $b = 4.572$ Å. c) Illustration of a possible configuration of Sn atoms (white circles connected with red lines) on the Co surface (black disks connected with black lines). The Sn atoms are shown to rest in hollow sites on the Co surface, whereby the lattices are rotated by 30° with respect to each other. The corresponding hollow site distance of 4.363 Å translates into a lattice mismatch of ≈5% with the relaxed α-Sn lattice. d,e) RHEED images of the Co(0001) layer for the sample oriented along two distinct symmetry axes rotated azimuthally by 30°, as indicated by red and blue arrows. f,g) Corresponding RHEED images of an ≈3 nm thick α-Sn(111) layer along the same azimuths, showing roughly a doubling of the lattice constant compared to Co and the 30° rotation between the Co and Sn layers. The solid lines represent the positions of the Co RHEED streaks, and the dashed lines in the Sn RHEED images the corresponding positions for a 5% increased lattice constant, suggesting that the α-Sn film is partially (or fully) relaxed.

template on *a*-plane Al_2O_3.[53,54] A 15–20 nm thick Co layer was subsequently deposited and the quality of the Co layer was monitored during growth using reflection high-energy electron diffraction (RHEED). Figure 1d,e shows RHEED images of a complete Co layer with the sample oriented in two azimuthal orientations differing by 30°, confirming the high quality of the Co layer. The two distinct RHEED patterns repeat every 60°, confirming the sixfold symmetry of the Co surface. For further verification of the quality of the Co layer, the samples were capped with Si and their magnetic properties were determined using vector network analyzer (VNA) FMR.

For the Sn growth, it is advantageous to reduce the substrate temperature to the lowest value possible and use a low Sn flux. In our molecular beam epitaxy (MBE) system, which is equipped with a cryo-shroud for the cells and the substrate heater, the lowest substrate temperature is $\approx$20 °C with the Sn cell at growth temperature ($\approx$1020 °C). The Sn deposition was monitored by taking RHEED images every 30 s. It was found that deposition of Sn initially resulted in clear RHEED images with streaks corresponding to a doubling of the lattice constant compared to the Co layer (compare Figure 1d,e,f,g). With increasing thickness of the Sn layers, the images became blurry and diffraction spots appeared, indicative of 3D growth. We conducted a systematic growth series whereby the Sn growth was terminated after a given time, and the topography of the sample was studied using atomic force microscopy (AFM). Figure S1, Supporting Information, shows that thin Sn layers are indeed flat, yet beyond a critical thickness of $\approx$3 nm, pillars start to form, which can grow as high as a couple of hundred nanometers. Further, given the different orientations in which α-Sn can grow on Co(0001), the films are characterized by a granular texture.

For the spin-pumping experiments, a spin-valve structure was prepared. The nominal Sn layer thickness was 2 nm and therefore below the critical thickness for the formation of 3D structures. A 5 nm thick magnetic Py layer was deposited onto the Sn layer, and the sample subsequently capped with amorphous Si to prevent oxidation. The complete heterostructure is as follows: Si/Py(5)/Sn(2)/Co(15)/Au(23)/Mo(13)/Al_2O_3 (the numbers in parentheses denote thicknesses in nanometers). The structural properties of the spin-valve structures were further analyzed using X-ray reflectivity (XRR), AFM, and high-resolution transmission electron microscopy (HRTEM), as well as high-angle annular dark-field scanning transmission electron microscopy (HAADF-STEM).

To determine the phase transition temperatures in Sn thin films on Co, which are very sensitive to strain in the thin films,[13] we performed XRR in the temperature range between 80 and 300 K. The XRR data are shown in **Figure 2**a. Apart from continuous shift of the fringes with temperature, no qualitative change is observed that would indicate the occurrence of the α→β phase transition. Due to the complex layer structure of the spin-valve samples, and the small thickness of the Sn layer, it was difficult to determine its quality from the analysis of the X-ray data alone. We have therefore conducted electron microscopy on the spin-valve stack and the respective HRTEM and HAADF-STEM images are shown in Figure 2b,c. From the analysis of these images, the thicknesses of the core layers are as follows: $t_{\mathrm{Co}} = (14.1 \pm 1.2)$ nm, $t_{\mathrm{Sn}} = (2.6 \pm 0.8)$ nm, and $t_{\mathrm{Py}} = (4.9 \pm 0.5)$ nm. The chemical composition of the individual layers was determined using energy-dispersive spectroscopy (EDS).

The magnetic properties of the samples were studied by conducting FMR experiments. VNA-FMR measurements were performed for frequencies in the range 0.5–20 GHz, for in-plane magnetic fields ranging from 0 to 300 mT, and for temperatures from 80 to 347 K. Frequency-field plots obtained at 80, 300, and 347 K are shown in **Figure 3**a–c. Comparison of the plots leads to the conclusion that a change in temperature mostly affects the magnetic anisotropy of the Co layer, whereby the FMR frequency is higher at higher temperatures. As a consequence, the Co and Py layer resonances separate more clearly at higher temperatures. The complete data sets are shown in Figure S2, Supporting Information.

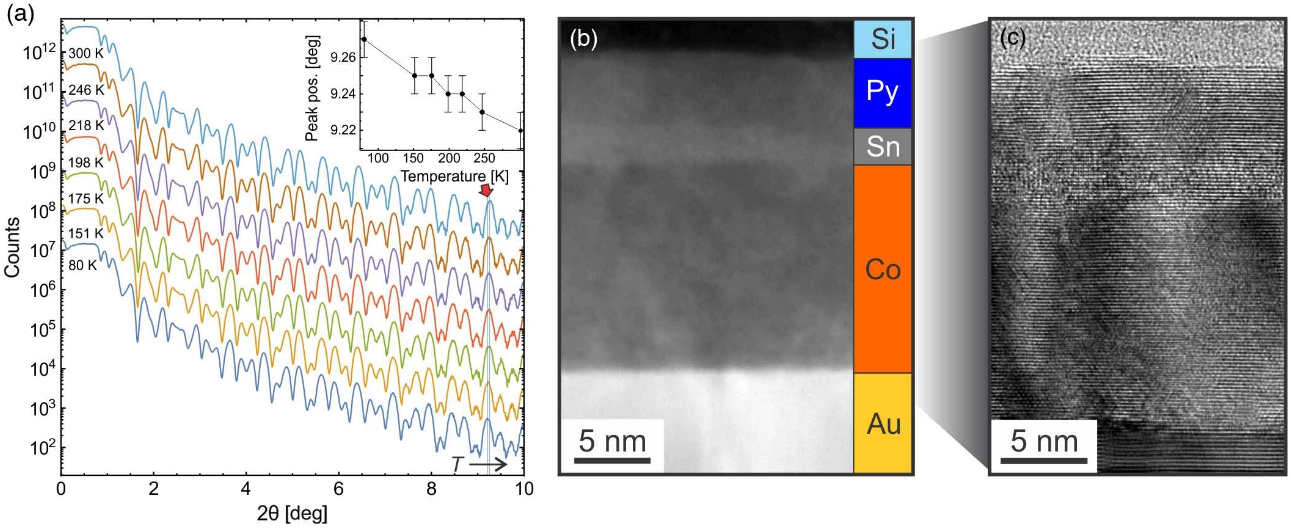

Figure 2. a) XRR measurements performed in the temperature range between 80 and 300 K. The plots are vertically shifted for clarity. The shift of the last peak (indicated by the red arrow) with temperature is shown in the inset. b) HAADF-STEM and c) HRTEM images of the spin-valve heterostructure.

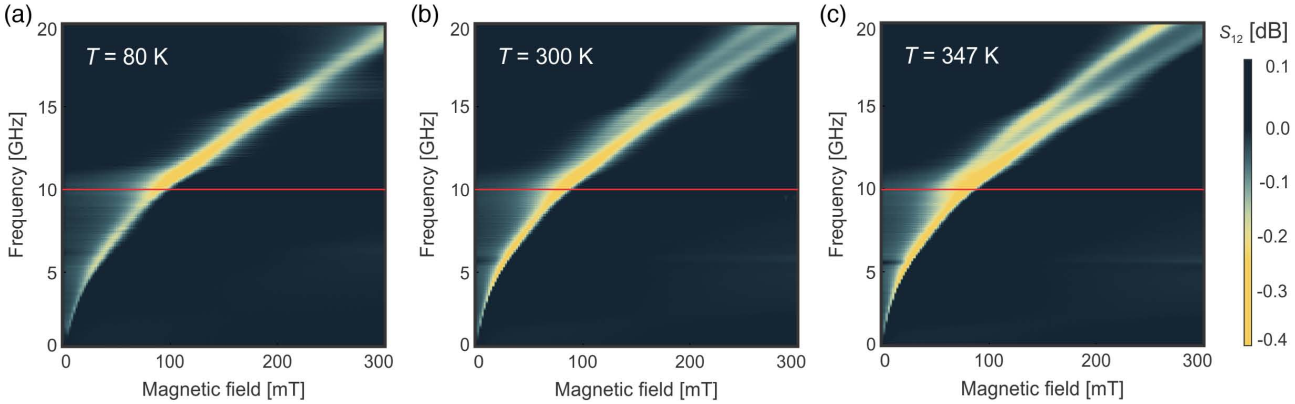

Figure 3. a–c) VNA-FMR measurements (of S_{12} [dB]) at 80 K (a), 300 K (b), and 347 K (c) with the magnetic field oriented in the sample plane. The red line at 10 GHz indicates the frequency at which the XFMR measurements were conducted.

3. XFMR Measurements and Model Fitting

The observed VNA-FMR spectra arise from microwave absorption in both magnetic layers. However, to gain insight into the dynamics of the individual magnetic layers, and thereby measure spin pumping through the spin-valve structure, time- and element-resolved XFMR is required.[55] In our XFMR experiment, the sample is placed face down onto a coplanar waveguide (CPW), above a small hole in the center of the transmission line. This allows the excitation of the sample with a microwave current and, at the same time, for the illumination of the sample with circularly polarized X-rays (as shown in **Figure 4**a). XFMR makes use of the X-ray magnetic circular dichroism (XMCD) effect, i.e., the dependence of the absorption of circularly polarized X-rays on the sample magnetization direction. With the X-ray energy tuned to either the Co or Fe L_3 absorption edge, each of the magnetic layers can be probed separately.

The XFMR experiments were performed with a driving frequency of 10 GHz and in a temperature range between 80 and 328 K. The surface normal of the sample was oriented at an angle of 55° with respect to the beam direction and the external magnetic field was applied in the sample plane. In a synchrotron measurement, the X-rays arrive periodically in bunches. Time resolution is achieved by performing stroboscopic measurements of the precession of the magnetization vector. For carrying out such delay scans, the phase difference between the incoming beam pulses and the driving microwave oscillations are varied. The phase and amplitude of the oscillations are obtained by fitting a sine function of the form $X\sin(2\pi f t) + Y\cos(2\pi f t)$ to the delay scan data. This form of the fitted function is chosen for its statistical properties, as it allows for the simple estimation of uncertainties (as discussed in Gladczuk et al.,[34]). Selected (X, Y) plots are shown in Figure 4b,e. The X and Y data can be converted into the more intuitive amplitude and phase representation using Equation (9) in Gladczuk et al.[34] and these plots are shown in Figure 4c–d,f–g below the (X, Y) plots. The data sets for all temperatures are shown in Figure S3, Supporting Information.

As the investigated spin-valve structure is composed of two magnetic layers, two resonance modes are expected. If the layers are magnetically uncoupled, each of these resonances is associated with the precession of one of the layers. This is clearly not the case for the acquired XFMR data (Figure 4). For the spin-valve structure, a twin resonance peak is observed, which is very clearly distinguishable at 328 K. This is an indication that both modes involve oscillations of both magnetic layers, which means that they are coupled. Note, however, that the larger peak splitting at higher temperatures is not caused by a change in coupling strength between the layers, but rather by a change in the anisotropy of the Co layer.

Two major types of coupling can be distinguished, Heisenberg-type exchange coupling (EC) and spin-current-mediated coupling (SC). The first type of coupling occurs when the magnetic thin films are in close proximity to each other. SC, in contrast, requires the pumping of a spin current from the layer at resonance into the other magnetic layer.[34] SC is normally a small effect compared to exchange coupling, and hard to unambiguously confirm. In FMR, the appearance of SC will lead to the broadening of the resonance curve, while EC coupling will affect the position of the resonance, having the strongest effect for low magnetic fields. In contrast, using XFMR, the presence of a coherent pure spin current can be directly confirmed by detecting the phase and amplitude of precession of the second layer in the spin-valve structure, which is not excited at resonance.[33]

Recently, we have reported a small spin-pumping effect in a MgO-based magnetic tunnel junction using XFMR and here we apply the same methodology to the analysis of the Sn-based spin valves.[34] A theoretical model based on the Landau–Lifshitz–Gilbert–Slonczewski equation was fitted to the experimental XFMR data. For the fitting procedure, the values of the gyromagnetic ratios were fixed to $\gamma_{\mathrm{Co}} = 240\,000\,\mathrm{m s^{-1} A^{-1}}$ and $\gamma_{\mathrm{Py}} = 232\,000\,\mathrm{m s^{-1} A^{-1}}$. Two scenarios were considered. First, we assumed that the interlayer coupling is purely due to Heisenberg-type EC, and, second, both EC and SC were taken into account.[27] Both scenarios were compared using the likelihood-ratio test with the goal of determining if the addition of the SC term is necessary and justified. The likelihood-ratio test is a statistical tool that allows for the quantification of the validity of two competing models by their ability to describe the observed data more accurately. For this test, the likelihood of the best fit

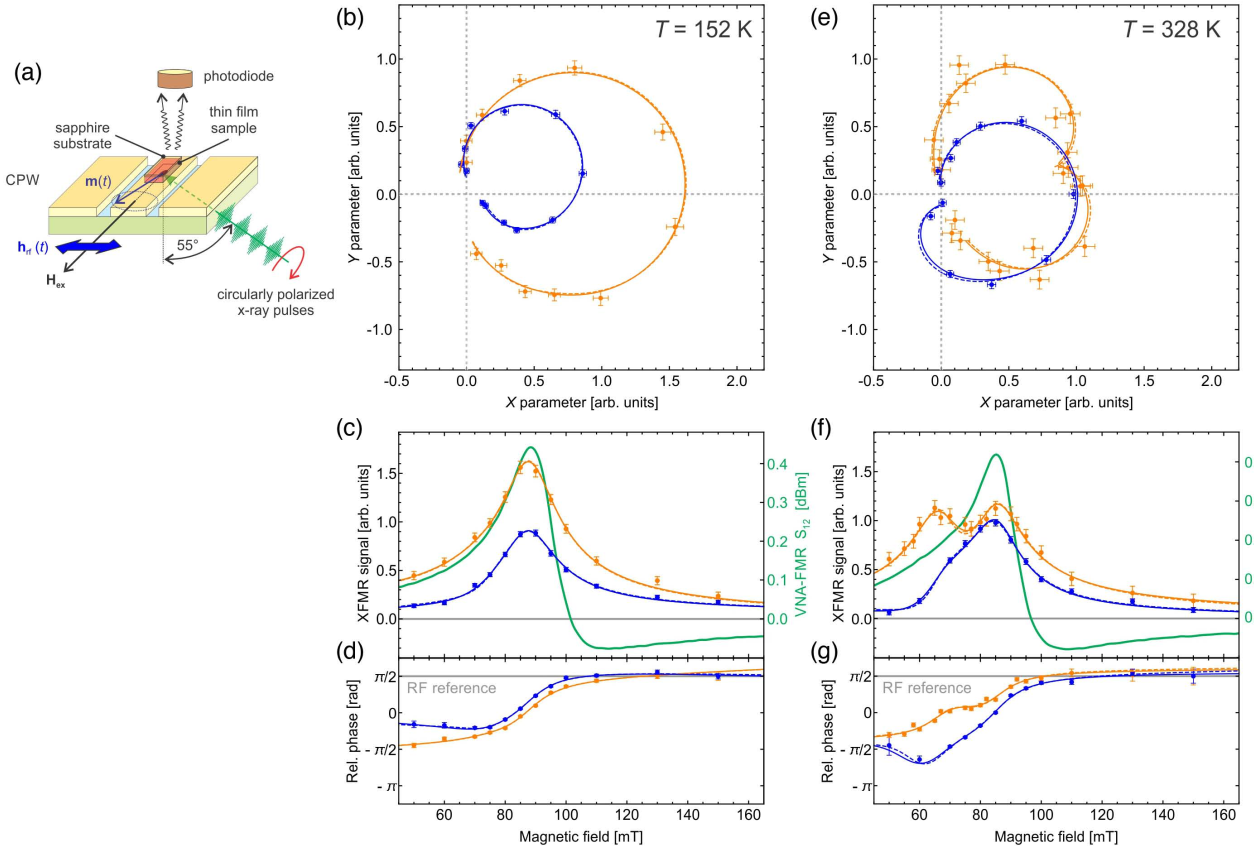

Figure 4. a) XFMR sample geometry. The sample is mounted with its long axis along the waveguide (the (0001)-axis of the *a*-plane sapphire substrate). b–g) Model fits to the XFMR data shown in the (X,Y)-plane (b,e), and the corresponding amplitude (c,f) and phase (d,g) plots as a function of the applied field. The experimental data are shown as solid circles for the Co (orange) and Py (blue) layers; the dashed lines represent the EC-only model fit, and the solid lines the SC&EC model fit. Here, fits to data taken at 152 K (b–d) and 328 K (e–g) are shown. The green lines represent the corresponding VNA-FMR signal (shown on a log scale) measured at a frequency of 10 GHz, at the same temperature as the XFMR results were obtained.

for each model is evaluated and their ratio is calculated. As the experimental data are subject to random noise, the resulting likelihood ratio is a random variable whose distribution can be approximated by a χ^2 distribution (subject to conditions as given in Wilks' theorem[56]). This allows for the estimation of the confidence of the test, the *P*-value. The resulting values of the EC coupling parameter (J), the likelihoodratios (λ_{LR}), and the corresponding *P*-values were determined assuming a χ_1^2 distribution, and are shown for both scenarios in **Table 1**. The *P*-values denote the probability of obtaining a goodness of the fit (likelihood) of at least the same value as the one obtained for the alternative model (SC&EC), assuming the EC-only model is correct. A high value of λ_{LR} would indicate that this scenario is very unlikely, and therefore rules in favor of the SC&EC model. Assuming a χ_1^2 distribution, a significance level of 5% (*P*-value) is obtained for $\lambda_{\mathrm{LR}} = 3.84$, meaning that the data are well described by the EC-only model if $\lambda_{\mathrm{LR}} < 3.84$. It is important to bear in mind that this is the significance level of the test and not that of the models. Further, note that a λ_{LR} of 5.41, as for the measurement at 328 K, is not a proof for spin pumping; it is only a coincidental event within a set of multiple measurements. Instead, the fact that low values of λ_{LR} were obtained in several measurements speaks in favor of the EC-only model. Also, the fluctuating values in Table 1 are not expected to arise from a temperature dependence, but instead from the statistics. Because λ_{LR} is a result of measurements that are subject to uncertainty, it can be treated as a random variable, whose probability distribution is approximated by χ_1^2. In such a case, it is expected that the values

Table 1. Values of the exchange coupling constants obtained from fitting the EC model to the XFMR data. The value of the likelihood-ratio test λ_{LR} is obtained by comparing the likelihood (goodness of the fit) of the SC&EC model to the likelihood of the EC-only model. The *P*-value corresponding to the respective λ_{LR} is shown in the P_{χ^2} column.

Temp [K]	J [mT]	λ_{LR}	P_{χ^2}
80	2.5 ± 1.1	1.26	0.26
152	2.6 ± 1.4	3.31	0.07
199	6.5 ± 2.5	0.06	0.80
218	6.4 ± 2.8	3.30	0.07
246	4.2 ± 1.0	0.38	0.54
300	4.8 ± 0.6	0.01	0.94
328	4.8 ± 2.1	5.41	0.02

of λ_{LR} are occasionally exceeding a value of 3.84. The data shown in Table 1 need to be interpreted collectively, e.g., using a one-sided Kolmogorv–Smirnov (KS) test to verify if the resulting λ_{LR} values follow the χ_1^2 distribution. For the data displayed in Table 1, the KS test returns a P-value of 26%; i.e., the λ_{LR} values obtained from the experimental data could have been obtained from the process following a χ_1^2 distribution (at 5% significance level).

Overall, it can be concluded that the inclusion of the SC term is not justified, i.e., that the EC term alone is sufficient to describe the coupling in the system and that addition of SC does not improve the fits significantly.

4. Conclusion

We have successfully grown α-Sn thin films on the surface of a magnetic material, thereby opening the door for the spintronic exploration of α-Sn. Using hcp Co(0001) as a virtual substrate, well-ordered and relaxed α-Sn layers were grown up to a critical thickness of ≈3 nm. Above this thickness, 3D growth is observed. The time- and layer-resolved XFMR measurements show two FMR modes, stemming from the Co and Py layers. Theoretical model optimization allowed for determination of the exchange coupling parameter J, which was in the range between 2.5 and 6.5 mT. By comparing this value with an MgO interlayer–based magnetic tunnel junction of similar thickness ($J_{\text{MgO}} \approx 1.0\,\text{mT}$), it can be concluded that α-Sn spin valves exhibit much stronger exchange coupling between the magnetic layers. The likelihood-ratio test of a model with and without spin pumping coupling gives λ_{LR} values that do not suggest the presence of spin pumping in the system. Due to the small thickness of the α-Sn layer, which is effectively a 2D-TI with chiral edge states, spin pumping through the layer is strongly suppressed. It should be noted, however, that the graininess of the Sn film could in fact support chiral edge states tied to each grain.[57] This should lead to an enhancement of the pumped spin current by many orders of magnitude (assuming a probed area of $100 \times 100\,\mu\text{m}^2$ and a grain size between 10 and 100 nm). However, even in the 3D-TI state, where spin pumping relies on surface instead of edge states, spin pumping is a small effect as we have previously shown in epitaxial FM/TI/FM systems.[37] One route forward is to optimize the Sn growth conditions by adjusting the substrate temperature or fine-tuning the deposition rates in the various stages of the Sn film growth. Finally, it is worth exploring the growth on other ferromagnetic alloys in which the lattice constant can be precisely tuned to also strain the α-Sn layer.

5. Experimental Section

For the growth of the hcp Co(0001) layer, Au (23 nm)/Mo (13 nm) heterostructure templates on *a*-plane sapphire were used as a virtual substrate. The $Al_2O_3(11\bar{2}0)$ substrates measured $5 \times 10\,\text{mm}^2$, with the [0001] direction parallel to the long side. The templates were grown by MBE at the Institute of Physics, Polish Academy of Sciences, and transported to Diamond Light Source (Didcot, UK). After loading, the samples were annealed at 500 K in the analysis chamber until the surface quality was recovered as monitored by low-energy electron diffraction (LEED) and XPS. Subsequently, the samples were transferred in vacuo into the MBE growth chamber (Createc), and a 15 nm thick Co layer was grown at 400 °C at a deposition rate of $0.016\,\text{nm s}^{-1}$. The sample temperature was then lowered (and kept at) room temperature for the remainder of the deposition process. Next, a 0–5 nm thick Sn film was grown. For the spin-valve structures, a second ferromagnetic Py layer was grown at a rate of $0.0025\,\text{nm s}^{-1}$ by codeposition out of a Ni and an Fe effusion cell. Finally, the films were capped with a layer of amorphous Si to prevent oxidation, yet thin enough to allow for soft X-ray spectroscopy. The films were structurally characterized in situ using rRHEED and LEED, and their composition by XPS. Ex situ XRR (Cu Kα_1 source with $\lambda = 1.5406$ Å) and AFM (see Figure S1, Supporting Information) were used to determine the thicknesses of the ferromagnetic layers and the surface morphology, respectively. The interface and crystalline quality of the heterostructures was investigated using HRTEM as well as HAADF-STEM, equipped with an EDS detector (EDS data not shown). The magnetic properties were studied using a superconducting quantum interference device (SQUID) vibrating sample magnetometry (VSM) system and VNA FMR. Time-resolved X-ray detected FMR (XFMR) experiments were conducted in a portable octupole magnet system (POMS) on beamline I10 at the Diamond Light Source. Element-specific XMCD was used to add element, and hence layer, specificity to the FMR experiment. XFMR enables the determination of the time time-resolved precession of the magnetization of an FM layer undergoing FMR.[37,55,58] Phase-resolved measurements were performed by synchronizing the driving RF signal with the storage ring master-oscillator clock (500 MHz). The measured RMS jitter was <5 ps, much less than the X-ray pulse length (≈35 ps). Measurements were performed at driving frequencies up to 10 GHz; higher frequencies were excluded as they required delay steps between RF excitation and X-ray probe below the measured jitter. The X-ray absorption in the sample was monitored using the X-ray excited optical luminescence (XEOL) yield from the Al_2O_3 substrate, detected by a photodiode placed directly behind the sample. The time-dependent signal was measured using lock-in detection. For details on the statistical analysis of the XFMR data, the reader is referred to Gladczuk et al.[34]

Supporting Information

Supporting Information is available from the Wiley Online Library or from the author.

Acknowledgements

The authors acknowledge the Diamond Light Source for beamtime on I10 under proposal numbers SI-15211 and SI-16099, and the Research Complex at Harwell for their hospitality. Ł.G. was supported through a joint studentship between the Diamond Light Source and the University of Oxford (support by the Engineering and Physical Sciences Research Council through a doctoral training award).

Conflict of Interest

The authors declare no conflict of interest.

Data Availability Statement

The data that support the findings of this study are available from the corresponding author upon reasonable request.

Keywords

ferromagnetic resonance, spin pumping, topological insulators, topological quantum materials

Received: March 10, 2021
Revised: April 8, 2021

---

[1] L. Fu, C. L. Kane, E. J. Mele, *Phys. Rev. Lett.* **2007**, *98*, 106803.
[2] J. E. Moore, *Nature* **2010**, *464*, 194.
[3] C. L. Kane, E. J. Mele, *Phys. Rev. Lett.* **2005**, *95*, 146802.
[4] B. A. Bernevig, T. L. Hughes, S.-C. Zhang, *Science* **2006**, *314*, 1757.
[5] J. E. Moore, L. Balents, *Phys. Rev. B* **2007**, *75*, 121306.
[6] R. Roy, *Phys. Rev. B* **2009**, *79*, 195322.
[7] Y. L. Chen, J. G. Analytis, J.-H. Chu, Z. K. Liu, S.-K. Mo, X. L. Qi, H. J. Zhang, D. H. Lu, X. Dai, Z. Fang, S. C. Zhang, I. R. Fisher, Z. Hussain, Z.-X. Shen, *Science* **2009**, *325*, 178.
[8] Y. L. Chen, J. H. Chu, J. G. Analytis, Z. K. Liu, K. Igarashi, H. H. Kuo, X. L. Qi, S. K. Mo, R. G. Moore, D. H. Lu, M. Hashimoto, T. Sasagawa, S. C. Zhang, I. R. Fisher, Z. Hussain, Z. X. Shen, *Science* **2010**, *329*, 659.
[9] D. Kong, Y. Cui, *Nat. Chem.* **2011**, *3*, 845.
[10] S. S. Hong, J. J. Cha, D. Kong, Y. Cui, *Nat. Commun.* **2012**, *3*, 757.
[11] D. Zhang, H. Wang, J. Ruan, G. Yao, H. Zhang, *Phys. Rev. B* **2018**, *97*, 195139.
[12] O. Madelung, *Semiconductors: Data Handbook*, Springer, Berlin/Heidelberg, Germany **2004**.
[13] K. Houben, J. K. Jochum, D. P. Lozano, M. Bisht, E. Menéndez, D. G. Merkel, R. Rüffer, A. I. Chumakov, S. Roelants, B. Partoens, M. V. Milošević, F. M. Peeters, S. Couet, A. Vantomme, K. Temst, M. J. V. Bael, *Phys. Rev. B* **2019**, *100*, 075408.
[14] R. F. C. Farrow, *J. Vac. Sci. Technol. B* **1983**, *1*, 222.
[15] T. Osaka, H. Omi, K. Yamamoto, A. Ohtake, *Phys. Rev. B* **1994**, *50*, 7567.
[16] H. Song, J. Yao, Y. Ding, Y. Gu, Y. Deng, M.-H. Lu, H. Lu, Y.-F. Chen, *Adv. Eng. Mater.* **2019**, *21*, 1900410.
[17] M. Cardona, *Solid State Commun.* **1967**, *5*, 233.
[18] Q. Barbedienne, J. Varignon, N. Reyren, A. Marty, C. Vergnaud, M. Jamet, C. Gomez-Carbonell, A. Lematre, P. Le Fèvre, F. Bertran, A. Taleb-Ibrahimi, H. Jaffrès, J.-M. George, A. Fert, *Phys. Rev. B* **2018**, *98*, 195445.
[19] C.-Z. Xu, Y.-H. Chan, Y. Chen, P. Chen, X. Wang, C. Dejoie, M.-H. Wong, J. A. Hlevyack, H. Ryu, H.-Y. Kee, N. Tamura, M.-Y. Chou, Z. Hussain, S.-K. Mo, T.-C. Chiang, *Phys. Rev. Lett.* **2017**, *118*, 146402.
[20] V. A. Rogalev, F. Reis, F. Adler, M. Bauernfeind, J. Erhardt, A. Kowalewski, M. R. Scholz, L. Dudy, L. B. Duffy, T. Hesjedal, M. Hoesch, G. Bihlmayer, J. Schäfer, R. Claessen, *Phys. Rev. B* **2019**, *100*, 245144.
[21] M. R. Scholz, V. A. Rogalev, L. Dudy, F. Reis, F. Adler, J. Aulbach, L. J. Collins-McIntyre, L. B. Duffy, H. F. Yang, Y. L. Chen, T. Hesjedal, Z. K. Liu, M. Hoesch, S. Muff, J. H. Dil, J. Schaefer, R. Claessen, *Phys. Rev. B* **2018**, *97*, 075101.
[22] M. Z. Hasan, C. L. Kane, *Rev. Mod. Phys.* **2010**, *82*, 3045.
[23] M. R. Scholz, J. Sánchez-Barriga, D. Marchenko, A. Varykhalov, A. Volykhov, L. V. Yashina, O. Rader, *Phys. Rev. Lett.* **2012**, *108*, 256810.
[24] L. A. Wray, S.-Y. Xu, Y. Xia, D. Hsieh, A. V. Fedorov, Y. S. Hor, R. J. Cava, A. Bansil, H. Lin, M. Z. Hasan, *Nat. Phys.* **2011**, *7*, 32.
[25] C.-Z. Chang, J. Zhang, X. Feng, J. Shen, Z. Zhang, M. Guo, K. Li, Y. Ou, P. Wei, L.-L. Wang, Z.-Q. Ji, Y. Feng, S. Ji, X. Chen, J. Jia, X. Dai, Z. Fang, S.-C. Zhang, K. He, Y. Wang, L. Lu, X.-C. Ma, Q.-K. Xue, *Science* **2013**, *340*, 167.
[26] T. Yokoyama, J. Zang, N. Nagaosa, *Phys. Rev. B* **2010**, *81*, 24.
[27] Y. Tserkovnyak, A. Brataas, G. E. W. Bauer, B. I. Halperin, *Rev. Mod. Phys.* **2005**, *77*, 1375.
[28] B. Heinrich, Y. Tserkovnyak, G. Woltersdorf, A. Brataas, R. Urban, G. E. W. Bauer, *Phys. Rev. Lett.* **2003**, *90*, 187601.
[29] A. Brataas, Y. Tserkovnyak, G. E. W. Bauer, B. I. Halperin, *Phys. Rev. B* **2002**, *66*, 060404.
[30] Y. Tserkovnyak, A. Brataas, G. E. W. Bauer, *Phys. Rev. B* **2002**, *66*, 224403.
[31] J.-C. Rojas-Sánchez, S. Oyarzún, Y. Fu, A. Marty, C. Vergnaud, S. Gambarelli, L. Vila, M. Jamet, Y. Ohtsubo, A. Taleb-Ibrahimi, P. Le Fèvre, F. Bertran, N. Reyren, J.-M. George, A. Fert, *Phys. Rev. Lett.* **2016**, *116*, 096602.
[32] J. Ding, C. Liu, Y. Zhang, V. Kalappattil, R. Yu, U. Erugu, J. Tang, H. Ding, H. Chen, M. Wu, *Adv. Funct. Mater.* **2021**, *31*, 2008411.
[33] M. K. Marcham, L. R. Shelford, S. A. Cavill, P. S. Keatley, W. Yu, P. Shafer, A. Neudert, J. R. Childress, J. A. Katine, E. Arenholz, N. D. Telling, G. van der Laan, R. J. Hicken, *Phys. Rev. B* **2013**, *87*, 180403.
[34] L. Gladczuk, L. Gladczuk, P. Dluzewski, K. Lasek, P. Aleshkevych, D. M. Burn, G. van der Laan, T. Hesjedal, *Phys. Rev. B* **2021**, *103*, 064416.
[35] J. Tian, I. Childres, H. Cao, T. Shen, I. Miotkowski, Y. P. Chen, *Solid State Commun.* **2014**, *191*, 1.
[36] A. R. Mellnik, J. S. Lee, A. Richardella, J. L. Grab, P. J. Mintun, M. H. Fischer, A. Vaezi, A. Manchon, E.-A. Kim, N. Samarth, D. C. Ralph, *Nature* **2014**, *511*, 449.
[37] A. A. Baker, A. I. Figueroa, L. J. Collins-McIntyre, G. van der Laan, T. Hesjedal, *Sci. Rep.* **2015**, *5*, 7907.
[38] D. A. Arena, E. Vescovo, C.-C. Kao, Y. Guan, W. E. Bailey, *Phys. Rev. B* **2006**, *74*, 064409.
[39] A. A. Baker, A. I. Figueroa, D. Pingstone, V. K. Lazarov, G. van der Laan, T. Hesjedal, *Sci. Rep.* **2016**, *6*, 35582.
[40] D. T. Wang, N. Esser, M. Cardona, J. Zegenhagen, *Surf. Sci.* **1995**, *343*, 31.
[41] J. T. Ryu, M. Katayama, K. Oura, *Surf. Sci.* **2002**, *515*, 199.
[42] B. R. Cuenya, M. Doi, W. Keune, *Surf. Sci.* **2002**, *506*, 33.
[43] W. Tu, Ph.D. thesis, University of Tennessee, Knoxville, TN, USA **2014**.
[44] M. Jäger, C. Brand, A. P. Weber, M. Fanciulli, J. H. Dil, H. Pfnür, C. Tegenkamp, *Phys. Rev. B* **2018**, *98*, 165422.
[45] T. Ichikawa, *Surf. Sci.* **1984**, *140*, 37.
[46] F. Ronci, S. Colonna, A. Cricenti, G. L. Lay, *J. Phys.: Condens. Matter* **2010**, *22*, 264003.
[47] R. Cortés, A. Tejeda, J. Lobo-Checa, C. Didiot, B. Kierren, D. Malterre, J. Merino, F. Flores, E. G. Michel, A. Mascaraque, *Phys. Rev. B* **2013**, *88*, 125113.
[48] W. Srour, A. Tejeda, M. Stoffel, M. Abun, Y. Fagot-Revurat, P. L. Fèvre, A. Taleb-Ibrahimi, D. Malterre, *J. Electron Spectrosc. Relat. Phenom.* **2014**, *195*, 174.
[49] B. F. Mason, B. R. Williams, *Surf. Sci.* **1992**, *262*, 169.
[50] A. Barfuss, L. Dudy, M. R. Scholz, H. Roth, P. Höpfner, C. Blumenstein, G. Landolt, J. H. Dil, N. C. Plumb, M. Radovic, A. Bostwick, E. Rotenberg, A. Fleszar, G. Bihlmayer, D. Wortmann, G. Li, W. Hanke, R. Claessen, J. Schäfer, *Phys. Rev. Lett.* **2013**, *111*, 157205.
[51] L. Marick, *Phys. Rev.* **1936**, *49*, 831.
[52] N. Oehl, G. Schmuelling, M. Knipper, R. Kloepsch, T. Placke, J. Kolny-Olesiak, T. Plaggenborg, M. Winter, J. Parisi, *CrystEngComm* **2015**, *17*, 8500.
[53] L. Gladczuk, P. Aleshkevych, R. Szymczak, P. Dluzewski, M. Aleszkiewicz, W. Paszkowicz, R. Minikayev, P. Przyslupski, *J. Appl. Phys.* **2009**, *105*, 063907.
[54] L. Gladczuk, M. Aleszkiewicz, *Thin Solid Films* **2013**, *539*, 372.
[55] G. van der Laan, *J. Electron Spectrosc. Relat. Phenom.* **2017**, *220*, 137.

[56] S. S. Wilks, *Ann. Math. Stat.* **1938**, *9*, 60.

[57] M. Dc, R. Grassi, J.-Y. Chen, M. Jamali, D. Reifsnyder Hickey, D. Zhang, Z. Zhao, H. Li, P. Quarterman, Y. Lv, M. Li, A. Manchon, K. A. Mkhoyan, T. Low, J.-P. Wang, *Nat. Mater.* **2018**, *17*, 800.

[58] G. B. G. Stenning, L. R. Shelford, S. A. Cavill, F. Hoffmann, M. Haertinger, T. Hesjedal, G. Woltersdorf, G. J. Bowden, S. A. Gregory, C. H. Back, P. A. J. de Groot, G. van der Laan, *New J. Phys.* **2015**, *17*, 013019.